PHYSICAL REVIEW A **77**, 043803 (2008)

Experimental and theoretical study of dynamical hysteresis and scaling laws in the polarization switching of vertical-cavity surface-emitting lasers

Jon Paul,[1] Cristina Masoller,[2] Paul Mandel,[3] Yanhua Hong,[1] Paul S. Spencer,[1] and K. Alan Shore[1]
[1]*School of Electronics, University of Wales, Bangor, Dean Street, Bangor LL57 1UT, Wales, United Kingdom*
[2]*Departament de Física i Enginyeria Nuclear, Universitat Politècnica de Catalunya, Colom 11, E-08222 Terrassa, Spain*
[3]*Université Libre de Bruxelles, Optique Nonlinéaire Théorique, Campus Plaine Code Postal 231, B-1050 Bruxelles, Belgium*

(Received 12 November 2007; published 1 April 2008)

We study experimentally the role of the bias current sweep rate in measurements of polarization switching (PS) of vertical-cavity surface-emitting lasers. We find that the size of the hysteresis cycle of the PS for increasing and decreasing current follows a power-law relationship with the speed of the current ramp. A similar relation is found for the laser turn-on. Numerical calculations based on the spin-flip model are in good agreement with the observations. We also show that the PS points and the power-law exponents depend critically on the noise level included in the simulations.

DOI: 10.1103/PhysRevA.77.043803 PACS number(s): 42.55.Px, 42.60.Mi, 42.65.Sf

I. INTRODUCTION

Hysteresis phenomena are ubiquitous in nature and have been extensively studied in nonlinear bistable optical systems [1–9]. The size of the hysteresis cycle obtained when a system variable is plotted vs a periodically time-varying parameter often depends on the sweep rate of the parameter. Increasing the sweep rate usually results in larger hysteresis cycles because the bifurcation point is delayed [10]. Recently we studied this delay in the polarization switching points (PS) of vertical-cavity surface-emitting lasers (VCSELs), numerically in [11] and experimentally in [12]. Here we focus on the effect of the sweep rate on the size of the PS hysteresis cycle.

Due to anisotropies that break the circular transverse symmetry, the output of a VCSEL is linearly polarized along one of two orthogonal directions. When the VCSEL begins to lase one linear polarization dominates, and when the injection current is increased, it is observed in many devices that at a certain value of the injection current, μ_1, the emission switches to the orthogonal linear polarization [13]. Hysteresis usually occurs because when the current is decreased the PS occurs at a current value μ_2 that is different from that for the upward scan, μ_1. Moreover, the PS is often accompanied by complex polarization dynamics that can include polarization coexistence, polarization hopping, and the emission of elliptically polarized light [14–22].

In [11] the delay of the PS points due to the injection current sweeping rate was studied numerically. The injection current was varied linearly, $\mu(t)=\mu_i+bt$ for the forward sweep and $\mu(t)=\mu_f-b(t-\Delta T)$ for the downward sweep, where $b=(\mu_f-\mu_i)/\Delta T$ is the sweep rate, μ_i and μ_f are the initial and final values of the current ramp ($\mu_i<\mu_f$), and ΔT is the time interval during which the current increases or decreases. The influence of the sweep rate b on the PS points μ_1 and μ_2 was analyzed, and it was found that μ_1 (μ_2) increases (decreases) when b increases. Thus, fast current ramps enlarge the hysteresis cycle since the switching point moves to higher current values for increasing injection and to lower current values for decreasing injection. A power-law relationship was also found for the times when the bifurcations take place, t_1^* and t_2^*, measured from the minimum and maximum of the current ramp, respectively, $t_1^*=(\mu_1-\mu_i)/b$ for increasing current and $t_2^*=(\mu_f-\mu_2)/b$ for decreasing current. A relationship of the form $t_{1,2}^*\propto b^{-\alpha}$ with $\alpha\simeq 0.95<1$ was found and experiments performed in [12] confirmed this numerical prediction.

An issue that remained to be explored is whether a scaling law exists for the size of the PS hysteresis cycle, $A=|\mu_1-\mu_2|$, and if there is one, if the exponent is the same as that observed for the laser turn-on-turn-off hysteresis cycle, since the PS and the turn-on are bifurcations that arise from different types of instabilities. We find experimentally that the size of the cycle A increases with the frequency of the triangular ramp, $\Omega=1/(2\Delta T)$ as $A=A_s+\Omega^{\alpha}$, where A_s is the size of the static hysteresis cycle. The static cycle occurs when changing the control parameter adiabatically; as an example, in the case of the laser turn-on-turn-off cycle $A_s=0$ because when the bias current varies adiabatically the laser turns on and off at the same current value. We find similar values of the exponent α for the turn-on-turn-off cycle and the PS cycle (0.74 and 0.69, respectively). Numerical simulations of the spin-flip model [23–25] give results consistent with this observation. However, they also reveal a critical influence of noise.

This paper is organized as follows. Section II describes the experimental setup and presents measurements of the turn-on and PS points for various frequencies of the triangular signal used to modulate the injected current. Section III describes briefly the spin-flip model and presents the results of the simulations. Section IV presents the conclusions.

II. EXPERIMENTS

The experimental setup, shown in Fig. 1, is the same as in [12]. A commercial single-longitudinal-mode VCSEL was driven by an ultralow noise current source and was temperature controlled to within 0.01 K. The laser output was collimated using an antireflection coated laser diode objective lens. The half-wave plate (HWP) and polarization beam splitters (PBS) were used to direct the orthogonal polarization components of the VCSEL to detectors D1 and D2. Two

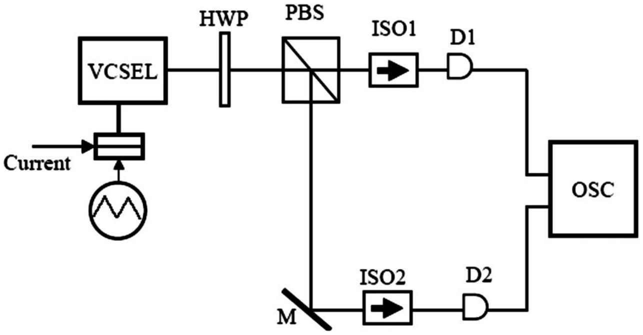

FIG. 1. Schematic diagram of experimental arrangement. HWP, half-wave plate; PBS, polarization beam splitter; ISO1 and ISO2, optical isolators; D1 and D2 photodetectors; M, mirror; and OSC, oscilloscope.

optical isolators (ISO1 and ISO2) with more than −40 dB isolation were used to prevent light feedback from the detectors into the VCSEL. The outputs from the detectors were stored in a 1 GHz bandwidth digital oscilloscope (OSC). The current supplied to the laser was controlled by a signal generator and a triangular modulation signal (of amplitude 0.45 mA peak-to-peak) was added to the VCSEL through the current source. The voltage on the laser changed from 1.55 mV to 2.0 mV. The frequency of the modulating signal was varied to study the influence of the speed of the current ramp.

At threshold the output of the laser is linearly polarized in one direction, defined as the X polarization. When the bias current is increased above a certain value, it is observed that the polarization switches to the orthogonal polarization (defined as the Y polarization). The turn-on point and the polarization switching points for increasing and decreasing current depend on the speed of the current ramp, as shown in Figs. 2(a) and 2(b), which display the polarization-resolved $L-I$ curve for several cycles of the modulating signal, for a slow and a fast current ramp, respectively.

The lasing turn-on, indicated with a circle, is defined as the injection current for which the intensity of the X polarization reaches a given value (in Fig. 2, $I_{th}=0.005$). The PS points for increasing and decreasing current, indicated with triangles and squares, respectively, are defined as the input for which the intensity of the suppressed polarization suddenly grows from the noise level and crosses a given value (in Fig. 2, $I_{PS}=0.0125$). I_{th} and I_{PS} are slightly different because the intensity of the suppressed mode continues to increase after the laser turns on (see Fig. 2, where the black line indicates a constant zero level).

Because the turn-on and the PS are stochastic processes driven by noise, for the various cycles of the modulating signal the turn-on and polarization switching events occur at slightly different values of the injection current, and thus, there is a small dispersion of the symbols that indicate these points.

If the current ramp is slow enough [Fig. 2(a)], the intensity traces for increasing and decreasing bias current superpose. The laser turns on for upwards current scans, and turns off for downwards current scans, at the same value of the bias current, equal to 1.8 mV. This value defines the "static" threshold, $J_{s,0}$. In Figs. 2(a) and 2(b), the horizontal axis represents the injection current normalized as $\mu=J/J_{s,0}$, i.e., such that $\mu_{0,s}=1$. The PS is not abrupt but is accompanied by polarization anticorrelated oscillations. The PS points for upwards and downwards current scans define the "static" bifurcation points, $\mu_{1,s}\sim 1.025$ and $\mu_{2,s}\sim 1.04$, respectively.

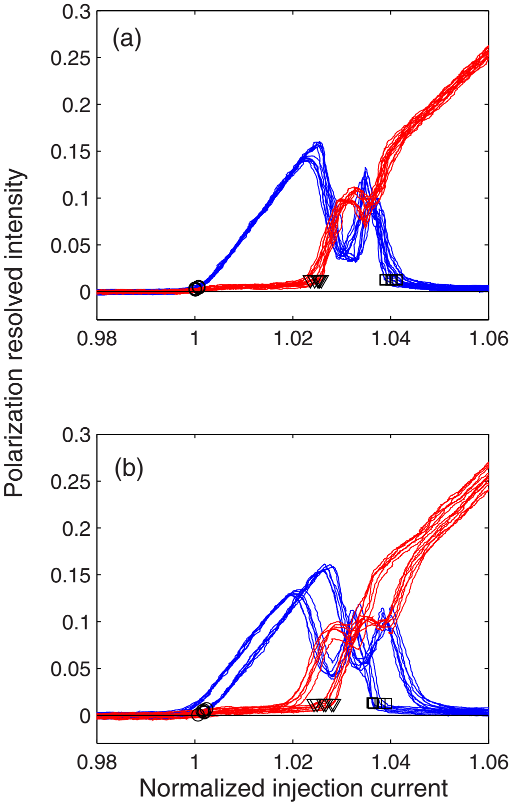

FIG. 2. (Color online) Polarization-resolved $L-I$ curve. The PS points for increasing current, for decreasing current, and the turn-on for increasing current are indicated by triangles, squares, and circles, respectively. The frequency of the modulating signal is (a) 120 Hz and (b) 1200 Hz.

For a faster current ramp [Fig. 2(b)], hysteresis is observed and the X- and Y-polarizations intensity traces for increasing and decreasing bias current do not superpose. In Fig. 3, we plot turn-on points versus the frequency of the current ramp. Lasing threshold occurs at μ_0; PS occurs at μ_1 (μ_2) for the upward (downward) part of the scan. Figure 3(a) reveals that μ_0 and μ_1 increase, while μ_2 decreases with increasing frequency, as reported previously in [11,12]. A plot of the size of the hysteresis cycle of the laser turn-on, $A_{th}=\mu_0-\mu_{0,s}$, vs the ramp frequency [Fig. 3(b), circles], and of the size of the PS hysteresis cycle minus the size of the static hysteresis cycle, $A_{PS}-A_{PS,s}=(\mu_1-\mu_2)-(\mu_{1,s}-\mu_{2,s})$, vs the ramp frequency [Fig. 3(b), triangles] reveals power-law relationships with exponents 0.74 and 0.69, respectively.

III. THEORY

In this section we present results of simulations using the spin-flip model [23–25] that are in good agreement with the observations. We also investigate the influence of noise.

The rate equations for the linearly polarized slowly varying complex amplitudes E_x and E_y, the total carrier density

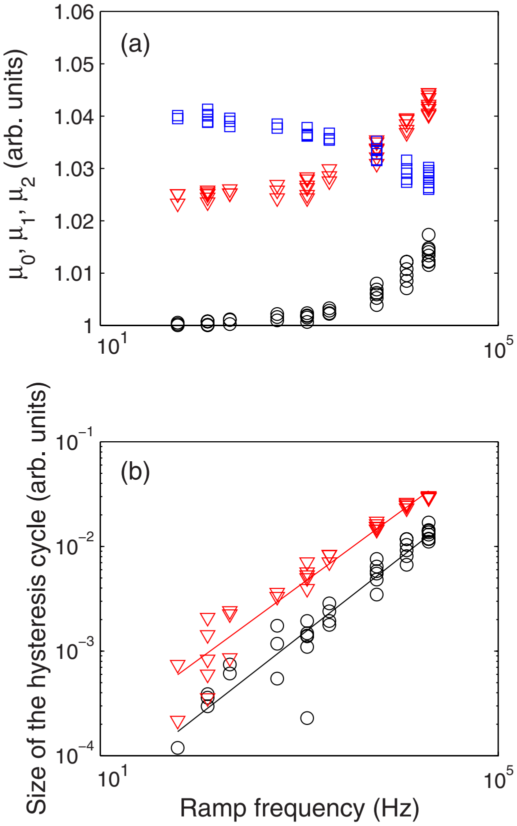

FIG. 3. (Color online) (a) Log-linear plot of the turn-on points (circles), PS points for increasing current (triangles), and decreasing current (squares), vs the *ramp* frequency. (b) Log-log plot of the size of the turn-on hysteresis cycle (circles) and of the PS cycle (triangles) vs the frequency of the ramp. The solid lines indicate the fit: $\ln(\mu_0-\mu_{0,s})=a\ \ln(f)+b$ with $a=0.74$ and $b=-11.7$, and $\ln[(\mu_1-\mu_2)-(\mu_{1,s}-\mu_{2,s})]=c\ \ln(f)+d$ with $c=0.69$ and $d=-10.3$.

$N=N_+ + N_-$, and the carrier difference $n=N_+ - N_-$ (where N_+ and N_- are two carrier populations with positive and negative spin value) are [24]

$$\dot{E}_{x,y} = k(1+j\alpha)[(N-1)E_{x,y} \pm jnE_{y,x}] \mp (\gamma_a + j\gamma_p)E_{x,y} + \sqrt{\beta_{sp}}\xi_{x,y}, \quad (1)$$

$$\dot{N} = \gamma_N[\mu(t) - N(1+|E_x|^2+|E_y|^2) + jn(E_yE_x^* - E_xE_y^*)], \quad (2)$$

$$\dot{n} = -\gamma_s n - \gamma_N[n(|E_x|^2+|E_y|^2) + jN(E_yE_x^* - E_xE_y^*)], \quad (3)$$

here k is the field decay rate, γ_N is the decay rate of the total carrier population, γ_s is the spin-flip rate, and α is the linewidth enhancement factor. γ_a and γ_p are linear anisotropies representing dichroism and birefringence, respectively [24]. γ_a leads to different gain-to-loss ratios and therefore to different thresholds for the two polarizations, with the y polarization having the lower threshold when γ_a is positive. γ_p leads to a frequency split between the two polarizations, with the x polarization having the lower frequency when γ_p is positive. β_{sp} is the strength of the spontaneous emission noise and $\xi_{x,y}$ are independent Gaussian white noise sources with zero mean and unit variance. μ is the injection current parameter, normalized such that the static lasing threshold is at $\mu_{0,s}=1$.

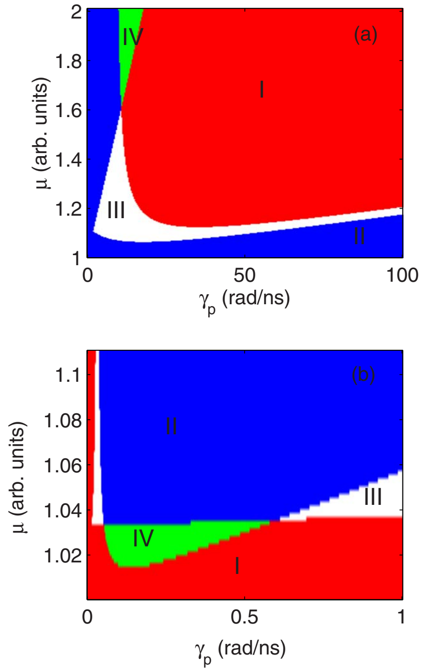

FIG. 4. (Color online) Numerically calculated stability regions for (a) positive dichroism ($\gamma_a=0.4\ \text{ns}^{-1}$) and (b) negative dichroism ($\gamma_a=-0.1\ \text{ns}^{-1}$). The Roman numerals indicate regions where (I) x is the only linear polarization stable; (II) y is the only linear polarization stable; (III) both linear polarizations are stable; and (IV) no linear polarization is stable.

The model has steady-state solutions corresponding to linearly polarized states. These are

$$E_x = \mathcal{E}_x e^{i\omega_x t}, \quad E_y = 0, \quad N = \mathcal{N}_x, \quad n = 0, \quad (4)$$

and

$$E_x = 0, \quad E_y = \mathcal{E}_y e^{i\omega_y t}, \quad N = \mathcal{N}_y, \quad n = 0, \quad (5)$$

where $\omega_{x,y} = \pm\alpha\gamma_a \mp \gamma_p$, $\mathcal{N}_{x,y} = 1 \pm \gamma_a/k$, and $\mathcal{E}_{x,y} = \sqrt{\mu/\mathcal{N}_{x,y} - 1}$. Solutions corresponding to elliptically polarized states also exist [24].

The stability of these solutions depends not only on the linear anisotropy parameters (γ_a,γ_p), but also on the spin-flip rate and phase-amplitude coupling. The linear stability analysis reveals that in the spin-flip model two types of PS exist; one is from the high frequency to the low frequency polarization and has been referred to in the literature as type I [26] ($y \rightarrow x$ if $\gamma_p - \alpha\gamma_a > 0$). This PS occurs for positive dichroism and large enough birefringence [$\gamma_p > \gamma_s/(2\alpha)$]. The other type of PS is from the low frequency to the high frequency polarization ($x \rightarrow y$ if $\gamma_p - \alpha\gamma_a > 0$), and occurs for negative dichroism and small birefringence ($\gamma_p < \gamma_s/(2\alpha)$, referred to as type II in [26]).

The two types of PS are associated with different bifurcation scenarios, as illustrated schematically in Fig. 4, which represents the linear stability of the x and y polarizations. In Fig. 4 the parameter space (γ_p,μ) is divided in four regions of different stability: in regions I and II only x- or y-polarized solutions are stable, respectively; in region III both linear polarizations are stable, and in region IV, both are unstable.

For parameters corresponding to type I PS [Fig. 4(a)] there is a region of bistability (III) in between regions I and II and thus, for increasing or decreasing μ while keeping γ_p fixed [i.e., moving upwards or downwards along a vertical line in Fig. 4(a)] the PS $y \to x$ ($x \to y$) occurs at the upper (lower) boundary of region III. Thus, the static bifurcation points for increasing and decreasing current, $\mu_{1,s}$ and $\mu_{2,s}$ respectively, are at the upper and at the lower boundary of region III, and are such that $\mu_{1,s} > \mu_{2,s}$.

However, in the experiments described in the previous section the opposite relation was observed, and this can be understood, within the framework of this model, by considering parameters for type II PS [Fig. 4(b)], and a small birefringence. In this region of parameter space, when increasing (decreasing μ) while keeping γ_p fixed a PS $x \to y$ ($y \to x$) occurs when going from region I to II (or from II to I) but in between these regions there is region IV where both linear polarizations are unstable. Thus, the static bifurcation points for increasing and decreasing current are at the boundaries of regions I and II, respectively, and now they are such that $\mu_{1,s} < \mu_{2,s}$.

We investigate the existence of scaling laws for the size of the hysteresis cycles in both types of PS. We solve numerically the model equations with typical VCSEL parameters: $k = 300$ ns^{-1}, $\alpha = 3$, $\gamma_n = 1$ ns^{-1}, $\gamma_s = 50$ ns^{-1}, and $\beta_{sp} = 10^{-6}$ ns^{-1}, unless otherwise stated. We start with type II PS, with linear anisotropy parameters (γ_a, γ_p) adjusted such the static PS points $\mu_{1,s}$ and $\mu_{2,s}$ are similar to the experimental values. We will show that scaling laws exist consistent with the experiments.

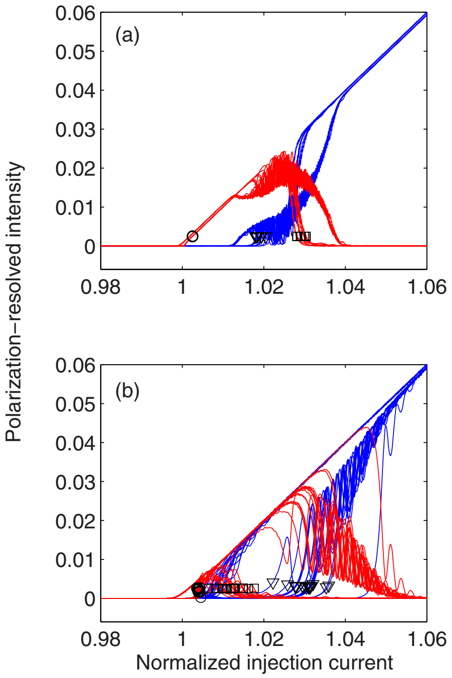

FIG. 5. (Color online) Numerically calculated polarization-resolved $L-I$ curve for parameters corresponding to type II PS: $\gamma_a = -0.1$ ns^{-1} and $\gamma_p = 0.15$ rad/ns. The frequency of the current ramp is (a) 10^{-4} GHz and (b) 10^{-3} GHz. The PS points for increasing current, for decreasing current, and the turn-on for increasing current are indicated by triangles, squares, and circles, respectively.

In a second step we will consider parameters (γ_a, γ_p) corresponding to type I PS. We will show that type I PS also exhibits scaling laws for the size of the hysteresis cycle vs the ramp frequency. Moreover, in contrast to type II PS, type I PS is abrupt and is not accompanied by polarization anticorrelated oscillations. This allows assessing in a more straightforward way the role of noise. Type II PS is accompanied by polarization oscillations, and thus the PS points are less influenced by the noise, because the oscillations play a role similar to the noise (i.e., they help driving the trajectory away from the unstable solution and toward the stable one). We will show that noise has a strong impact on type I PS, and in the exponent of the scaling law of the size of the hysteresis cycle.

A. Type II PS and comparison with the experiments

Figure 5 displays the numerically calculated $L-I$ curve for two different frequencies of the triangular signal that

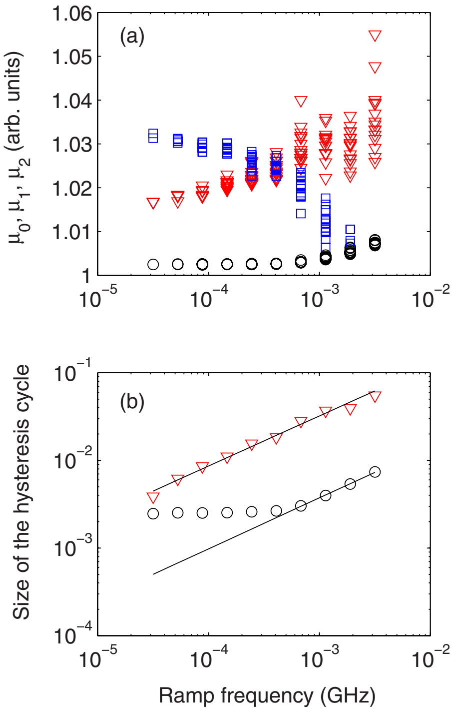

FIG. 6. (Color online) (a) Log-linear plot of the numerically calculated turn-on points (circles) and PS points for increasing current (triangles) and decreasing current (squares) vs the frequency of the ramp. (b) Log-log plot of the size of the turn-on hysteresis cycle (circles) and of the PS cycle (triangles) vs the frequency of the ramp. The solid lines indicate the fit: $\ln(\mu_0 - 1) = a \ln(f) + b$ with $a = 0.58$ and $b = -1.57$, and $\ln[(\mu_1 - \mu_2) - (\mu_{1,s} - \mu_{2,s})] = a \ln(f) + b$ with $a = 0.57$ and $b = 0.51$. Parameters correspond to type II PS: $\gamma_a = -0.1$ ns^{-1} and $\gamma_p = 0.15$ rad/ns.

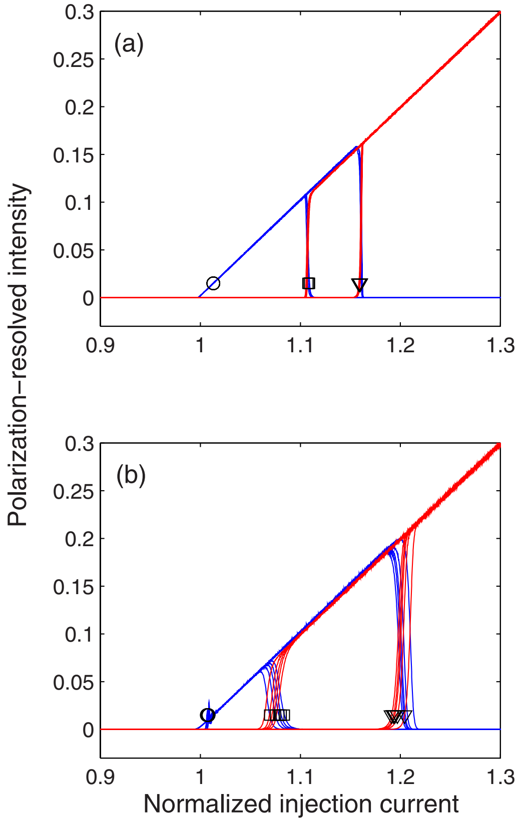

FIG. 7. (Color online) Numerically calculated polarization-resolved $L-I$ curve for parameters corresponding to type I PS: $\gamma_a=0.4\ \mathrm{ns}^{-1}$ and $\gamma_p=66\ \mathrm{rad/ns}$. The frequency of the current ramp is (a) 10^{-4} GHz and (b) 10^{-3} GHz. The PS points for increasing current, for decreasing current, and the turn-on for increasing current are indicated by triangles, squares, and circles, respectively.

changes the injection current parameter. The amplitude and the extreme values of the triangular signal were kept fixed and were chosen such as to fit the experimental situation. Because in the experiments the bias current was varied between 1.55 mV and 2.0 mV and the static lasing threshold occurred at about 1.8 mV, in the simulation the injection current parameter μ, that is, the current normalized to the static threshold, varies from $\mu_i=0.86$ to $\mu_f=1.11$.

Several cycles of the modulating signal are displayed. Because the PS occurs across a region of the parameter space where both polarizations are unstable, antiphased polarization oscillations accompany the PS. To simulate the finite bandwidth of the detectors used in the experiments, in the simulations the polarization oscillations have been smoothed out using an appropriate digital filter.

Figure 6(a) displays the numerically calculated turn-on and PS points μ_0, μ_1, and μ_2, vs the frequency of the current ramp. Figure 6(b) displays the size of the hysteresis cycle of the laser turn-on, $A_{th}=\mu_0-\mu_{0,s}$, vs the ramp frequency (circles), and the size of the PS cycle minus the size of the static cycle, $A_{PS}-A_{PS,s}=(\mu_1-\mu_2)-(\mu_{1,s}-\mu_{2,s})$, vs the ramp frequency (triangles). Power-law relationships are found, with exponents 0.58 and 0.57 for the turn-on cycle and the PS cycle, respectively, that are consistent with those found experimentally.

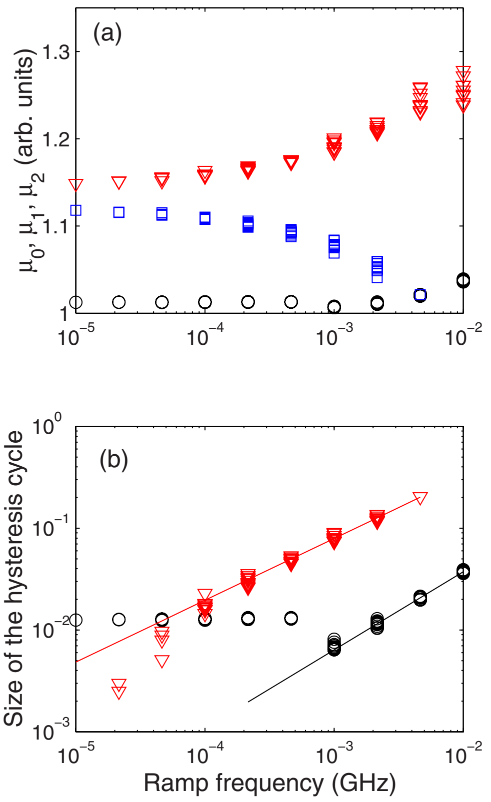

FIG. 8. (Color online) (a) Log-linear plot of the numerically calculated turn-on points (circles) and PS points for increasing current (triangles) and decreasing current (squares) vs the frequency of the ramp. (b) Log-log plot of the size of the turn-on hysteresis cycle (circles) and of the PS cycle (triangles) vs the frequency of the ramp. The solid lines indicate the fit: $\ln(\mu_0-1)=a\ln(f)+b$ with $a=0.77$ and $b=0.25$, and $\ln[(\mu_1-\mu_2)-(\mu_{1,s}-\mu_{2,s})]=a\ln(f)+b$ with $a=0.61$ and $b=1.66$. Parameters correspond to type I PS: $\gamma_a=0.4\ \mathrm{ns}^{-1}$ and $\gamma_p=66\ \mathrm{rad/ns}$.

B. Type I PS and the influence of noise

In this section we consider parameters corresponding to type I PS, and thus, as explained above, the static bifurcation points are such that $\mu_{1,s}>\mu_{2,s}$. The frequency of the triangular signal is varied while the amplitude of the triangular signal is kept fixed: $\mu_i=0.8<\mu_{0,s}$ and $\mu_f=1.6>\mu_{1,s}$. Figure 7 displays the numerically calculated $L-I$ curve for two different frequencies of the triangular signal. Several cycles of the modulated signal are shown. In contrast to type II PS analyzed in the previous section, there is a rather abrupt switch from one polarization to the orthogonal one.

Figure 8(a) displays the numerically calculated turn-on and PS points μ_0, μ_1, and μ_2, vs the frequency of the current ramp. Figure 8(b) displays the size of the hysteresis cycle of the laser turn-on, $A_{th}=\mu_0-\mu_{0,s}$, vs the ramp frequency (circles), and the size of the PS cycle minus the size of the static cycle, $A_{PS}-A_{PS,s}=(\mu_1-\mu_2)-(\mu_{1,s}-\mu_{2,s})$, vs the ramp frequency (triangles). Power-law relationships are found, with exponents 0.77 and 0.61 for the turn-on cycle and the PS cycle, respectively.

Our simulations show that there is a strong sensitivity to the level of noise. Not only the turn-on point, but also the PS

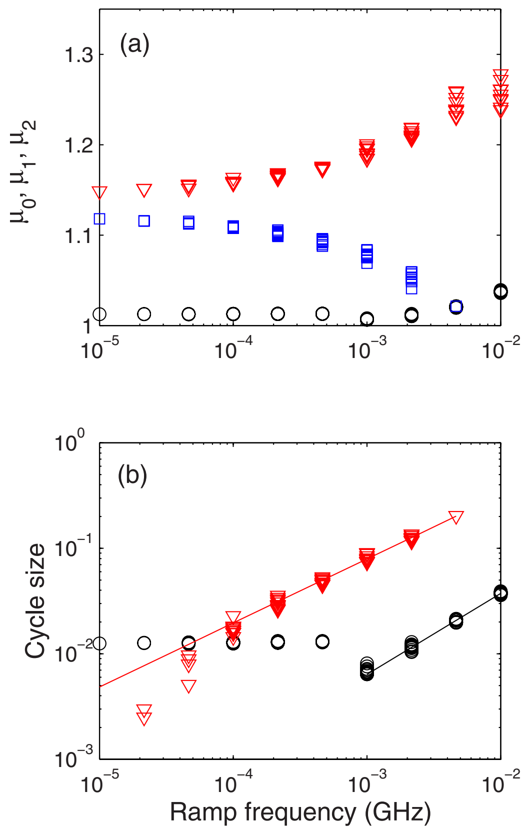

FIG. 9. (Color online) As in Fig. 5 but with $\beta_{sp}=10^{-5}$ ns^{-1}. The solid lines indicate the fit: $\ln(\mu_0-1)=a\ln(f)+b$ with $a=0.79$ and $b=0.29$, and $\ln(\mu_1-\mu_{1,s}+|\mu_2-\mu_{2,s}|)=a\ln(f)+b$ with $a=0.56$ and $b=1.15$.

points are strongly noise dependent. Figures 9 and 10 display results for the same parameters as before, but with higher and lower noise levels, respectively. The exponents of the power-law relations also depend on the noise [27]. Table I presents the exponents for various noise levels. With $\beta_{sp}=0$ the laser turns on and depending on the speed of the ramp a PS for upward scans might occur, but no PS was observed in the downward part of the scan, at least, for the range of ramp speeds considered, the initial conditions and ramp extreme values μ_i and μ_f, used in the simulations, that were kept fixed in all the simulations. This indicates that, for this model, the deterministic limit is a singular limit of limited relevance.

TABLE I. Exponents of power-law relationships vs noise strength.

β_{sp} (ns^{-1})	Turn-on cycle	PS cycle
10^{-5}	0.79	0.56
10^{-6}	0.77	0.61
10^{-16}	0.66	0.55
10^{-26}	0.62	0.54
10^{-36}	0.60	0.53
0	0.53	

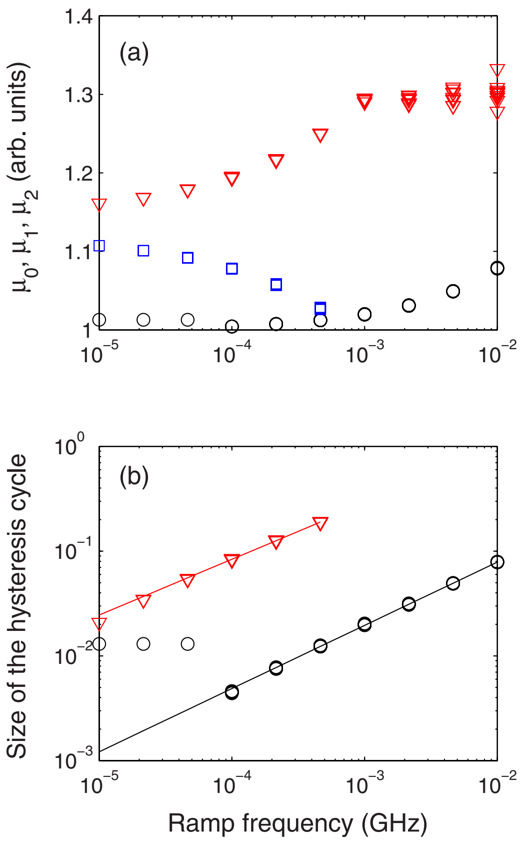

FIG. 10. (Color online) As in Fig. 5 but with $\beta_{sp}=10^{-36}$ ns^{-1}. The solid lines indicate the fit: $\ln(\mu_0-1)=a\ln(f)+b$ with $a=0.60$ and $b=0.24$, and $\ln(\mu_1-\mu_{1,s}+|\mu_2-\mu_{2,s}|)=a\ln(f)+b$ with $a=0.53$ and $b=2.42$.

IV. CONCLUSIONS AND DISCUSSION

We studied experimentally and numerically the influence of the bias current sweep rate on the turn-on and polarization switching (PS) hysteresis cycles of vertical-cavity surface-emitting lasers.

Experimentally, measurements of the polarization-resolved $L-I$ curve were performed. The current supplied to the VCSEL was controlled by a signal generator that provided a triangular signal of fixed amplitude and allowed one to scan the bias current from a value below threshold to a value above the PS point. By varying the frequency of the triangular signal it was found that the size of the hysteresis cycle of (i) the laser turn-on and turn-off for upwards and downwards scans and (ii) the PS points for upwards and downwards scans, both follow power-law relationships with the frequency of the current modulation [Fig. 3(b)].

Numerical simulations based on the spin-flip model show good agreement with the experimental observations. The spin-flip model presents two types of PS: from the high to the low frequency polarization (type I) and from the low to the high frequency polarization (type II). Type I and type II PS occur in different regions of the parameter space (shown schematically in Fig. 4), and have different characteristics. In type I PS there is an abrupt switch from one polarization to the orthogonal one. In between the regions of stable single linear polarization there is a region of bistability, and thus, the PS points for increasing and decreasing current are such that $\mu_1 > \mu_2$. In contrast, type II PS is not abrupt but is usually accompanied by polarization oscillations. If the birefringence parameter is small enough, in between the regions of stable single linear polarization there is a region of instability, where both linear polarizations are unstable, and thus, the PS points are such that $\mu_1 < \mu_2$. This type of PS resembles the experimental situation, where it was observed (Fig. 2) that the PS was accompanied by polarization oscillations and $\mu_1 < \mu_2$.

Numerically, we found scaling laws in both types of PS, with exponents consistent with those found experimentally. However, in the simulations a small value of birefringence parameter was needed in order to observe $\mu_1 < \mu_2$ as in the experiments. In the simulations, for type II PS, the frequency difference between the two polarizations is $(\gamma_p - \alpha\gamma_a)/\pi \sim 0.25$ GHz, and can be considered small in relation to typical values (of the order of a few to several gigahertz). We speculate that it is likely that in the VCSEL used in the experiments, light-matter interaction mechanisms not considered in the spin-model model (such as nonlinear anisotropies, higher-order contributions of the susceptibility function, four-wave mixing terms), are involved in the observed switching dynamics. Moreover, it is to be noticed that the time scales in the experiments and in the simulations differ by two or three orders of magnitude (compare the horizontal scales in Figs. 3 and 6). This difference can be attributed to slow mechanisms that are relevant in the experiments and are not included in the model, such as thermal effects (the shift of the gain curve and the cavity modes) and spatial effects (slow carrier diffusion and transverse hole burning). Both mechanisms are capable of inducing changes in the modal gains that can result in polarization switching [28,29].

We also investigated numerically the influence of noise. Because type II PS is accompanied by polarization oscillations, the type II PS points are less affected by noise: the oscillations play a role similar to noise by driving away the trajectory from the unstable solution and toward the stable one. In contrast, type I PS is rather abrupt, in general, not accompanied by oscillations, and thus, is more straightforward to assess the impact of noise. In type I PS the simulations show a critical role of noise in determining the turn-on point, the PS points, and the exponents of the power-law relationships (see Table I). A detailed investigation of the role of noise and its relation with various parameters is left for future work.

ACKNOWLEDGMENTS

J.P. acknowledges support from UK Engineering and Physical Sciences Research Council (EPSRC-GB) under Grant No. EP/C010612/1. C.M. acknowledges support from the “Ramon and Cajal” Program (Spain), the Spanish Ministerio de Educación y Ciencia through project No. FIS2005-07931-C03-03 and the U.S. Air Force Office of Scientific Research under Grant No. FA9550-07-1-0238. P.M. acknowledges support from the Fonds National de la Recherche Scientifique (Belgium). Y.H. acknowledges support from EPSRC-GB under Grant No. GR/S22936/01.

---

[1] P. Jung, G. Gray, R. Roy, and P. Mandel, Phys. Rev. Lett. **65**, 1873 (1990).
[2] A. Hohl, H. J. C. van der Linden, R. Roy, G. Goldsztein, F. Broner, and S. H. Strogatz, Phys. Rev. Lett. **74**, 2220 (1995).
[3] J. C. Celet, D. Dangoisse, P. Glorieux, G. Lythe, and T. Erneux, Phys. Rev. Lett. **81**, 975 (1998).
[4] S. H. Choi, E. White, D. M. Wood, T. Dodson, K. V. Vasavada, and G. Vemuri, Opt. Commun. **160**, 261 (1999).
[5] S. Sivaprakasam, D. N. Rao, and R. S. Pandher, Opt. Commun. **176**, 191 (2000).
[6] A. N. Pisarchik, B. F. Kuntsevich, R. Meucci, and E. Allaria, Opt. Commun. **189**, 313 (2001).
[7] J. R. Tredicce, G. L. Lippi, P. Mandel, B. Charasse, A. Chevalier, and B. Picque, Am. J. Phys. **72**, 799 (2004).
[8] A. Joshi, W. G. Yang, and M. Xiao, Opt. Lett. **30**, 905 (2005).
[9] A. Naumenko, N. Loiko, M. Sondermann, K. Jentsch, and T. Ackemann, Opt. Commun. **259**, 823 (2006).
[10] P. Mandel, *Theoretical Problems in Cavity Nonlinear Optics* (Cambridge University Press, England, 1997).
[11] C. Masoller, M. S. Torre, and P. Mandel, J. Appl. Phys. **99**, 026108 (2006).
[12] J. Paul, C. Masoller, Y. Hong, P. S. Spencer, and K. A. Shore, Opt. Lett. **31**, 748 (2006).
[13] C. J. Chang-Hasnain, J. P. Harbison, G. Hasnain, A. C. Vonlehmen, L. T. Florez, and N. G. Stoffel, IEEE J. Quantum Electron. **27**, 1402 (1991).
[14] T. Ackemann and M. Sondermann, Appl. Phys. Lett. **78**, 3574 (2001).
[15] L. Fratta, P. Debernardi, G. P. Bava, C. Degen, J. Kaiser, I. Fischer, and W. Elsässer, Phys. Rev. A **64**, 031803(R) (2001).
[16] J. Kaiser, C. Degen, and W. Elsässer, J. Opt. Soc. Am. B **19**, 672 (2002).
[17] S. Bandyopadhyay, Y. Hong, P. S. Spencer, and K. A. Shore, Opt. Commun. **202**, 145 (2002).
[18] B. Nagler, M. Peeters, J. Albert, G. Verschaffelt, K. Panajotov, H. Thienpont, I. Veretennicoff, J. Danckaert, S. Barbay, G. Giacomelli, and F. Marin, Phys. Rev. A **68**, 013813 (2003).
[19] J. Houlihan, D. Goulding, Th. Busch, C. Masoller, and G. Huyet, Phys. Rev. Lett. **92**, 050601 (2004).
[20] M. Holub, J. Shin, S. Chakrabarti, and P. Bhattacharya, Appl. Phys. Lett. **87**, 091108 (2005).
[21] G. Van der Sande, M. Peeters, M. I. Veretennicoff, J. Danckaert, G. Verschaffelt, and S. Balle, IEEE J. Quantum Electron. **42**, 898 (2006).
[22] A. Homayounfar and M. J. Adams, Opt. Express **15**, 10504 (2007).
[23] M. San Miguel, Q. Feng, and J. V. Moloney, Phys. Rev. A **52**, 1728 (1995).
[24] J. Martin-Regalado, F. Prati, M. San Miguel, and N. B. Abraham, IEEE J. Quantum Electron. **33**, 765 (1997).

[25] M. San Miguel, in *Semiconductor Quantum Optoelectronics*, edited by A. Miller, M. Ebrahimzadeh, and D. M. Finlayson (Institute of Physics, Bristol, 1999), p. 339.

[26] B. Ryvkin, K. Panajotov, A. Georgievski, J. Danckaert, M. Peeters, G. Verschaffelt, H. Thienpont, and I. Veretennicoff, J. Opt. Soc. Am. B **16**, 2106 (1999).

[27] H. Zeghlache, P. Mandel, and C. Van den Broeck, Phys. Rev. A **40**, 286 (1989).

[28] A. Valle, J. Sarma, and K. A. Shore, IEEE J. Quantum Electron. **31**, 1423 (1995).

[29] S. Balle, E. Tolkachova, M. San Miguel, J. R. Tredicce, J. Martin-Regalado, and A. Gahl, Opt. Lett. **24**, 1121 (1999).